J.-S. Lönnroth, V. V. Parail, G. Corrigan, D. Heading, G. Huysmans, A. Loarte, S. Saarelma, G. Saibene, S. Sharapov, J. Spence, and contributors to the EFDA-JET Workprogramme. 2003. Integrated predictive modelling of the effect of neutral gas puffing in ELMy H-mode plasmas. Plasma Physics and Controlled Fusion, volume 45, number 9, pages 1689-1711.

http://www.iop.org/journals/ppcf
http://stacks.iop.org/ppcf/45/1689

INSTITUTE OF PHYSICS PUBLISHING PLASMA PHYSICS AND CONTROLLED FUSION

Plasma Phys. Control. Fusion **45** (2003) 1689–1711 PII: S0741-3335(03)57701-6

Integrated predictive modelling of the effect of neutral gas puffing in ELMy H-mode plasmas

J-S Lönnroth[1], V V Parail[2], G Corrigan[2], D Heading[2], G Huysmans[3], A Loarte[4], S Saarelma[1], G Saibene[4], S Sharapov[2], J Spence[2] and contributors to the EFDA-JET Workprogramme

[1] Association EURATOM-Tekes, Helsinki University of Technology, PO Box 2200, 02015 HUT, Finland
[2] EURATOM/UKAEA Fusion Association, Culham Science Centre, Abingdon, Oxon OX14 3DB, UK
[3] Association EURATOM-CEA, CEA Cadarache, DRFC, Bâtiment 513, 13108 Saint-Paul-Lez-Durance, France
[4] EFDA Close Support Unit, c/o Max Planck Institut für Plasmaphysik, Boltzmannstrasse 2, 85748 Garching, Germany

Received 23 December 2002, in final form 2 April 2003
Published 19 August 2003
Online at stacks.iop.org/PPCF/45/1689

Abstract

The effect of neutral gas puffing in ELMy H-mode plasmas is studied using integrated predictive transport modelling, which is needed because of the strong link between the plasma core, the edge transport barrier and the scrape-off layer. Self-consistent results are obtained by coupling the one-dimensional core transport code JETTO with the two-dimensional edge code EDGE2D. In addition, magnetohydrodynamic (MHD) stability analysis is performed on the output of the transport simulations. The results of the MHD stability analysis is used to adjust MHD stability limits in the transport modelling, so that there is a feedback loop between the transport codes and the MHD stability codes. It is shown that strong gas puffing causes a sequence of causalities involving edge density, collisionality, bootstrap current, total edge current and magnetic shear, eventually triggering a transition from second to first ideal (or resistive) $n = \infty$ ballooning stability. Qualitatively, the transition from second to first ballooning stability resembles the experimentally observed transition from type I to type III ELMy H-mode with the accompanying increase in ELM frequency and deterioration of plasma confinement.

1. Introduction

It is well-known that the edge plasma parameters influence the plasma performance in many different ways. In the ELMy H-mode , which is considered a reference scenario for the international thermonuclear experimental reactor (ITER) and other burning plasma

experiments, the link between edge and core is controlled by the edge transport barrier (ETB), a thin layer of improved transport characteristics. Conventionally, the plasma core, the ETB and the scrape-off layer (SOL) have been treated separately in predictive modelling with the motivation that the physics is very different in these three regions. Indeed, it seems plausible that core transport is usually dominated by drift-type plasma turbulence resulting in profile stiffness, whereas anomalous transport in the ETB is reduced or even completely suppressed by strong shear in plasma rotation. The reduced transport at the edge generates a strong pressure gradient and a large edge current, both leading to periodic magnetohydrodynamic (MHD) instabilities accompanied by sharp increases of anomalous transport. These so-called edge localized modes (ELMs) are thought to be controlled by either kink/peeling or ballooning MHD instabilities [1–5]. Kink modes are current-driven instabilities with low toroidal mode numbers n, typically stabilized by the pressure gradient, whereas ballooning modes have higher mode numbers and are destabilized mainly by the edge pressure gradient. Finally, transport in the SOL is dominated by very fast losses along the field lines and by atomic physics processes, including interaction between the plasma and neutrals. In many studies, modelling of the plasma does not include simulation of the ETB and the SOL. Instead, the values of the relevant plasma parameters on top of the ETB are used as boundary conditions for core modelling.

However, both theory and experiments show that there is a strong link between the edge and the core, so that even a modest variation of the plasma parameters in one region can lead to a dramatic change in overall plasma performance. Profile stiffness is probably the best-known example of such a link between core transport and edge parameters [6]. Another example of a link between the core, the ETB and the SOL is the effect of gas puffing in type I ELMy H-mode plasma [7], which will be discussed extensively in this paper. An increase in the level of neutral gas puffing, for instance, triggers a transition from type I to type III ELMs in experiments. Due to the strong link between the core, the ETB and the SOL, integrated modelling of all three regions is needed in order to obtain self-consistent results.

It should be made clear that modelling the dynamics of ELMs in the fully integrated simulations of all three plasma regions is still beyond the scope of this paper. Here, plasma evolution between ELMs is modelled in a fully integrated way, whereas fully integrated modelling of the heat pulse propagation during ELMs will be undertaken at a later stage. The dynamics of ELMs is modelled in stand-alone simulations of ETB and core. In an ELMy H-mode plasma, the pressure gradient and the associated bootstrap current slowly build up until one of these two parameters reaches a critical level, whereby an ELM disruption occurs. Each ELM temporarily increases all transport coefficients in the pedestal region causing the pressure gradient and bootstrap current to drop back to a low level. The ELM cycle is repeated periodically, as illustrated in figure 1, which shows a possible scenario of ELMs triggered by a critical pressure gradient. In the fully integrated modelling presented in this paper, the plasma is allowed to evolve toward a steady state. MHD stability analysis is carried out, when the pressure gradient has evolved to an appropriate pre-ELM state or a steady state has been reached.

The integrated predictive transport modelling of ELMy H-mode JET plasmas presented in this paper has been performed using a suite of JET transport codes. Core modelling has been done with the 1.5D transport code JETTO [8], whose output is linked to a suite of MHD stability codes. Since core modelling alone is not sufficient, the edge transport code EDGE2D/NIMBUS [9] has been used for two-dimensional modelling of the SOL. Finally, both core and edge have been modelled self-consistently using COCONUT, a coupling of EDGE2D and JETTO.

The MHD stability analysis has been performed using the codes IDBALL, HELENA and MISHKA [10]. IDBALL and HELENA have been used for $n = \infty$ ballooning stability

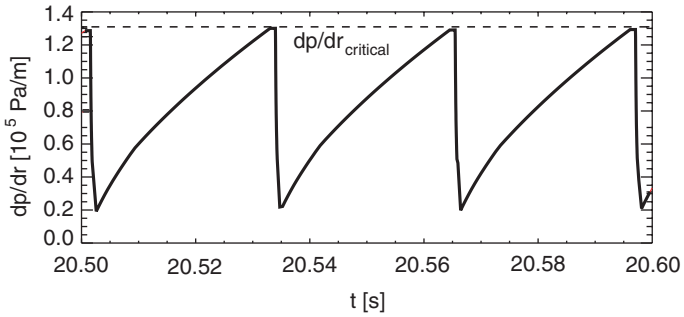

Figure 1. The pressure gradient as a function of time in a predictive JETTO simulation. In the model used here, it is assumed that the ELMs are triggered when the pressure gradient reaches a critical level. During an ELM, the pressure gradient drops back to the initial level and so the cycle repeats.

analysis. HELENA, which has an MHD equilibrium solver, also acts as a link between JETTO and MISHKA. Finally, MISHKA is used for kink/peeling and finite n ballooning stability analysis. To be specific, a version of MISHKA called MISHKA-1 is used in this study. This version is for ideal MHD and does not take into account the ω^* effect. The inclusion of drift effects [11] in the analysis will be discussed later.

The outline of this paper is as follows: the simulation model is described in section 2. In section 3, some experimental observations of relevance to this study are discussed. Section 4 is devoted to integrated predictive transport modelling. First, it is explained how integrated predictive modelling unravels a sequence of causalities which shows how strong gas fuelling can affect MHD stability. Some explanations for the experimental observations are proposed. Finally, integrated predictive transport modelling of a gas puffing scan is discussed in detail. Section 5 is devoted to MHD stability analysis of some of the scenarios from the gas puffing scan. The experimental observations outlined in section 3 are given possible explanations based on the modelling and MHD stability analysis. This paper is concluded with a short summary and discussion.

2. Simulation model

2.1. JETTO

In this work, the empirical JET transport model, a so-called mixed Bohm/gyro-Bohm model [12], has been used in simulations with JETTO, including integrated simulations with JETTO being part of the COCONUT code. The Bohm and the gyro-Bohm scalings in the JET model are given by relevant contributions to the diffusivity [13]. The Bohm term in the model includes both electron and ion transport as well as a non-local factor accounting for the global effect of perturbations starting at the plasma edge, such as the effect of ELMs on core transport. The gyro-Bohm term makes its largest contribution in the deep core. Some effects, the influence of which is rather negligible, are not included in the version of the JETTO transport model used in this work. For instance, sheared $\vec{E} \times \vec{B}$ flow is not accounted for, because its effect is small with unpeaked density profiles, as here. Momentum input is neglected, because it does not usually play a role in dense plasmas.

JETTO explicitly takes the region with the ETB into account. It is assumed that anomalous transport is completely suppressed within the ETB, so that the only remaining transport is

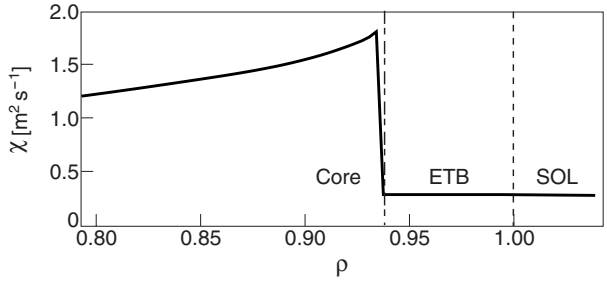

Figure 2. The ion transport coefficient χ_i as a function of the toroidal flux co-ordinate ρ in a typical COCONUT simulation with strong gas puffing ($\Gamma = 1 \times 10^{23}\,\mathrm{s}^{-1}$). In the core, a Bohm/gyro-Bohm model is used. Transport within the ETB is reduced to a neo-classical level. In integrated modelling with COCONUT and stand-alone edge modelling with EDGE2D, transport in the SOL is kept at a low neo-classical level as well.

neo-classical. The transport coefficients are thus suddenly reduced to the neo-classical level at the top of the ETB. This is illustrated in figure 2, which shows how the transport coefficients vary in the radial direction in a typical simulation. JETTO has a fixed boundary solver of the Grad–Schafranov equation, which generates equilibria consistent with the predicted temperature and pressure profiles in the core. The width of the ETB is considered either a fixed parameter or is calculated using recently developed theory-based models [14]. The effect of letting the pedestal width vary is studied in [15].

JETTO includes an implementation for dynamic modelling of ELMs [16]. Although the MHD stability code MISHKA can perform stability analysis against both kink and ballooning modes, ballooning stability is solely used as a trigger for ELMs in this paper. An ELM is triggered when the critical pressure gradient defined by an MHD stability limit is reached. In JETTO, one can specify a value for the normalized critical pressure gradient α_c. In this paper, the following normalization is used:

$$\alpha = -\frac{2\mu_0 q^2}{B_0^2 \epsilon}\frac{\mathrm{d}p}{\mathrm{d}\rho} \tag{1}$$

Here, μ_0 is permeability of vacuum, q is the safety factor, B_0 is the magnetic field on the magnetic axis, ϵ is the inverse aspect ratio, p is the pressure and ρ is the toroidal flux co-ordinate. During ELMs, all transport coefficients within the ETB are multiplied by given multiplication factors, here typically 100, during a given length of time, here typically 10^{-3} s. Even though the width of ballooning modes is only comparable to the width of the ETB, it makes sense to model transport in the ETB by a diffusive operator, because the individual harmonics forming the envelope of coupled harmonics have wavelengths and a correlation length much shorter than the ETB width. As discussed earlier, ELMs can also be triggered by current-driven kink modes. The latest version of JETTO includes an implementation for current-triggered ELMs as well, but in this paper it is assumed that the ELMs are controlled by the pressure gradient. Current-triggered ELMs will be considered elsewhere.

2.2. EDGE2D

The edge transport code EDGE2D works on a two-dimensional computational grid for the SOL. The grid covers the whole poloidal angle around the vacuum vessel as well as the target and private regions next to the divertor and the X-point. In stand-alone simulations with EDGE2D, the two-dimensional grid can be extended beyond the SOL to include the whole ETB. A typical

boundary condition in a stand-alone simulation is that the charged particle fluxes from the core into the simulation region equals the neutral particle fluxes from the simulation region into the core plus any assumed particle sources in the core. In addition, the heat fluxes at the boundary toward the core are given as boundary conditions. In stand-alone edge modelling with EDGE2D as well as in integrated modelling with COCONUT, perpendicular transport in the SOL is kept at the low neo-classical level, as shown in figure 2. Longitudinal transport is assumed to be classical.

Some justification can be given to the use of pure neo-classical transport in the SOL. Simulations with the orbit following code ASCOT [17] show evidence of a suppression of turbulent transport in the vicinity of the SOL [18]. The effect is felt of about one poloidal Larmor radius into the SOL, i.e. about 10 mm in outer midplane co-ordinates. Further outside the separatrix, transport is not suppressed to the neo-classical level. The suppression of turbulence occurs specifically in high-power H-modes in the inter-ELM period. In the simulations in this work, the SOL is very narrow, only about 15 mm at the midplane. In this narrow region, it is justifiable to use pure neo-classical transport. Since most of the power is deposited within the vicinity of the separatrix, modelling of the outer regions of the SOL is not undertaken in this paper.

2.3. COCONUT

In a coupled COCONUT run, the two-dimensional EDGE2D grid extends radially outward from the separatrix, whereas JETTO simulates the entire core region up to the separatrix in one dimension. Here, the width of the EDGE2D simulation region is typically about 1.5 cm at the midplane. The fact that the SOL is so narrow in the simulations does not affect the results significantly. The coupling of the codes is described in [19]. In a COCONUT run, JETTO calculates the heat fluxes and transport coefficients in the core and passes their values at the separatrix as boundary conditions for EDGE2D, whereas EDGE2D calculates the corresponding quantities in the SOL and passes their separatrix values as boundary conditions for JETTO. Both codes are called at each time step. Since the core is modelled in one dimension and the edge in two dimensions, the boundary conditions have to be treated as poloidally averaged. In a COCONUT run, the two-dimensional grid for EDGE2D extends a short distance inside the separatrix, so that there is a small overlap with the simulation region of JETTO. This makes it straightforward to distribute the one-dimensional heat fluxes and transport coefficients from JETTO uniformly over the whole poloidal angle for the JETTO-EDGE2D interface and to average the corresponding two-dimensional quantities from EDGE2D over the poloidal angle for JETTO. At the interface between JETTO and EDGE2D, the parallel velocity and the electric field are assumed to be zero. Parallel velocity and electric field then develop in the two-dimensional region, including the separatrix, where the full set of equations is solved by EDGE2D.

2.4. MHD stability codes

The MHD stability codes MISHKA and IDBALL are run using the output of stand-alone JETTO simulations. However, in order to keep the analysis self-consistent the separatrix values of, e.g. density and temperature from integrated self-consistent COCONUT runs are used as boundary conditions for the JETTO runs on which the MHD stability analysis is performed. The results of the MHD stability analysis, on the other hand, are used to set stability limits, e.g. an appropriate value for the critical pressure gradient, in modelling with JETTO and COCONUT. In this way, there is a feedback loop between the transport codes and

the MHD stability codes and the modelling can be considered integrated modelling of both transport and MHD stability.

3. Experimental background

The sensitive dependence of plasma performance on the edge parameters is very well demonstrated in experiments with external gas fuelling in type I ELMy H-mode plasma [7]. From experiments, it is known that plasma easily accommodates modest gas puffing, e.g. a neutral influx of $\Gamma = 3 \times 10^{22}\,\mathrm{s}^{-1}$ in the case of JET. Higher levels of gas puffing can trigger a transition from type I to type III ELMs with a dramatic increase in the ELM frequency followed by a deterioration of plasma confinement.

A comparison between JET discharges 53298 and 52739 can serve as an illustrative example. Both discharges are high-triangularity ($\delta = 0.5$) shots with very similar magnetic configurations. Figure 3 shows some characteristic time traces of the discharges. Frames (*a*), (*b*) and (*c*) contain the volume averaged electron density, the edge electron temperature and the thermal energy content, respectively. The underlying cause of the differences between the two discharges becomes apparent in the next few frames. As shown in frame (*d*) the heating power is essentially the same in both shots, $P_{\mathrm{tot}} = 16\,\mathrm{MW}$. Moreover, the magnetic field shown in frame (*e*) and the plasma current shown in frame (*f*) are also essentially the same in both discharges, $B_0 = 2.7\,\mathrm{T}$ and $I = 2.5\,\mathrm{MA}$, respectively. Hence, the major differences between the two shots are due to the different levels of external neutral gas fuelling shown in frame (*g*), $\Gamma = 0$ and $\Gamma = 6 \times 10^{22}\,\mathrm{s}^{-1}$ for shots 53298 and 52739, respectively. The different characteristics of the two discharges are perhaps best illustrated by comparing frames (*h*) and (*i*), which are time traces of D_α emission for shots 53298 and 52739, respectively. Shot 53298 with zero gas fuelling is characterized by low-frequency type I ELMs, whereas shot 52739 with strong gas fuelling features more frequent type III ELMs. The difference in ELM frequency is significant. The increased ELM frequency in discharge 52739 is accompanied by a deterioration of plasma confinement, as illustrated in frame (*j*) showing the confinement enhancement factor H98Y [20]. As will be shown, these experimental observations can be explained by integrated predictive modelling.

4. Results of integrated predictive transport modelling

4.1. Sequence of causalities unravelled by integrated predictive transport modelling

Integrated predictive transport modelling unravels a chain of causalities which might provide an explanation for the experimentally observed transition from type I to type III ELMs and the subsequent increase in ELM frequency. An increase in neutral gas puffing influences the SOL in the first place. To begin with, it should be understood that only a minor fraction of the total gas puff actually penetrates the separatrix.

The high-triangularity ELMy H-mode JET discharges 53298, 53299 and 52739 have been used as templates for a gas puff scan with the integrated code COCONUT. Shot 53299 differs from shots 53298 ($\Gamma = 0$) and 52739 ($\Gamma = 6 \times 10^{22}\,\mathrm{s}^{-1}$) only with respect to the level of gas puffing: $\Gamma = 5 \times 10^{22}\,\mathrm{s}^{-1}$ for shot 53299. For each level of neutral gas puffing, the total influx of neutral particles from the SOL through the separatrix into the core has been computed. The results of this study are shown in figure 4, which shows the total influx of neutrals through the separatrix as a function of the total puff rate. The figure reveals that as most of the neutrals are ionized in the SOL, only a small fraction of the total gas puff actually penetrates all the way through the separatrix. In fact, the neutral influx through the separatrix is between one

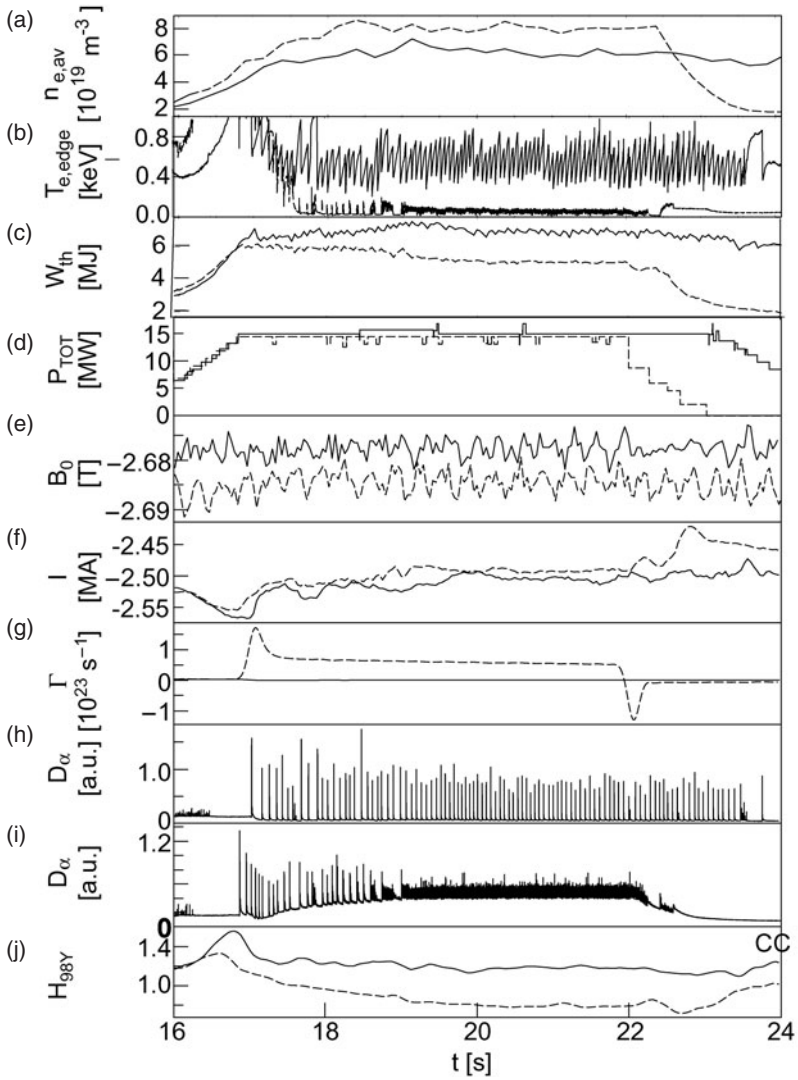

Figure 3. A comparison between JET discharges 53298 and 52739. The figure contains the following time traces: (*a*) Volume averaged electron density. (*b*) Edge electron temperature. (*c*) Plasma thermal energy content. (*d*) Neutral beam heating power. (*e*) Magnetic field. (*f*) Plasma current. (*g*) Neutral gas fuelling. (*h*) D_α emission in shot 53298. (*i*) D_α emission in shot 52739. (*j*) Confinement enhancement factor H98Y. In frames (*a*), (*b*), (*c*), (*d*), (*e*), (*f*), (*g*) and (*j*) the full line corresponds to shot 53298 and the dashed one to shot 52739.

and two orders of magnitude smaller than the total rate of gas fuelling and seems to decrease with increasing puff rate. This result is in line with [21, 22], which report that an increase in neutral density in the SOL creates an increase in plasma density that, in turn, increases the opacity to neutrals and results in reduced neutral penetration. The strong peak of neutral influx at the gas puff rate of $\Gamma = 6 \times 10^{22}\,\mathrm{s}^{-1}$ in figure 4 and reduction at $\Gamma = 4 \times 10^{22}\,\mathrm{s}^{-1}$ are artefacts, probably due to the limited accuracy of the method. The fact that the neutral influx is very small compared to the total gas puff might also contribute to the seemingly large fluctuation.

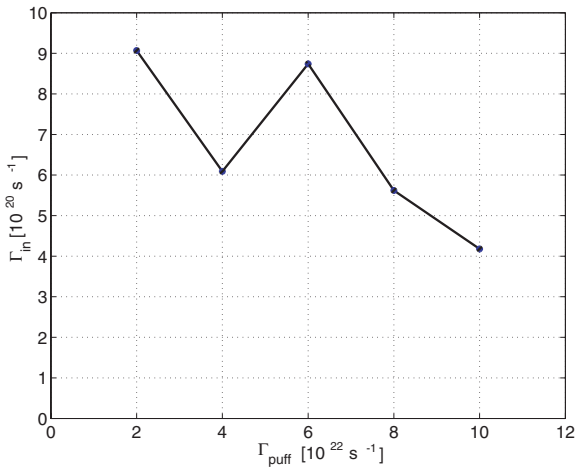

Figure 4. The total influx of neutrals through the separatrix as a function of the total rate of neutral gas puffing in integrated predictive simulations using the geometry of JET discharges 53298, 53299 and 52739.

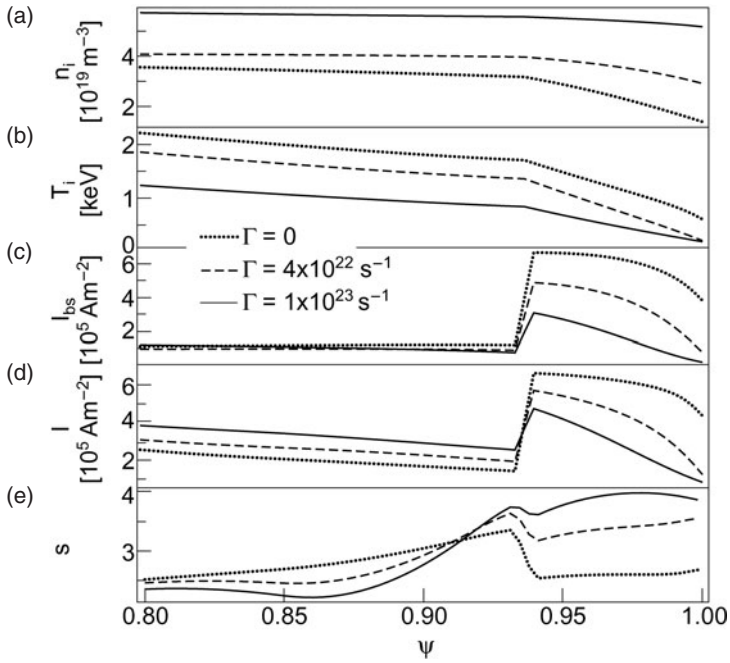

Figure 5. (*a*) Ion density, (*b*) ion temperature, (*c*) bootstrap current density, (*d*) total current density and (*e*) magnetic shear in three integrated predictive transport simulations with different levels of gas fuelling $\Gamma = 0$ (· · · · · ·), $\Gamma = 4 \times 10^{22}$ s^{-1} (- - - -) and $\Gamma = 1 \times 10^{23}$ s^{-1} (——).

The density in the vicinity of the separatrix increases sharply for increased gas puffing. Deeper in the core, the density increases much more slowly. The increase in density shown in frame (*a*) in figure 5. Figure 5, which illustrates a sequence of causalities revealed by integrated predictive modelling, contains the profiles of a number of relevant plasma parameters

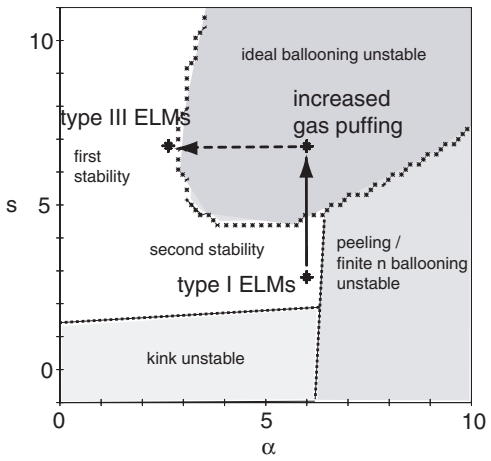

Figure 6. A typical MHD stability diagram with the normalized pressure gradient on the horizontal axis and magnetic shear on the vertical one. The region bounded by a rounded curve in the upper right-hand part of the figure is the ideal ($n = \infty$) ballooning unstable region. Predictive modelling shows that strong gas puffing can trigger a transition from second to first $n = \infty$ ballooning stability: increasing magnetic shear pushes the operational point into the ideal ballooning unstable region, whereby the pressure gradient drops due to the instability so that the operational point reaches the first stability region.

in three COCONUT runs with different levels of gas puffing: $\Gamma = 0$, $\Gamma = 4 \times 10^{22}\,\mathrm{s}^{-1}$ and $\Gamma = 1 \times 10^{23}\,\mathrm{s}^{-1}$. Frame (*b*) in figure 5 shows that both the temperature at the separatrix decreases for increasing gas puffing in order to keep the pressure and pressure gradient constant. Collisionality at the edge, on the other hand, increases with the edge density. To a first approximation, the bootstrap current I_{bs} scales as $I_{\mathrm{bs}} \sim 1/(1 + \nu^*)$, where ν^* is the collisionality. As a result of the increased collisionality at the edge, there is a significant decrease of the bootstrap current with increasing gas puffing, as shown in frame (*c*) in figure 5. Hence, the edge current, which comprises of both bootstrap and Ohmic current, decreases significantly, as illustrated in frame (*d*) in figure 5. Magnetic shear, plotted in frame (*e*) in figure 5, increases with decreasing edge current. It is known that magnetic shear controls MHD stability in general and ideal ($n = \infty$) ballooning stability in particular. In this way, external gas fuelling can play a significant role in controlling ballooning stability.

This effect on ballooning stability is illustrated in figure 6, which shows a typical $n = \infty$ ballooning stability diagram with the normalized pressure gradient on the horizontal axis and magnetic shear on the vertical one. The figure shows how predictive modelling might provide an explanation for the experimentally observed transition from type I to type III ELMs and increase in ELM frequency: increasing magnetic shear without changing the normalized pressure gradient causes the operational point to be pushed from the second ballooning stability region into the ideal ballooning unstable region. However, a real physical system cannot remain in a state with a combination of the pressure gradient and magnetic shear resulting in an instability. The emerging instability (ELM) should reduce the pressure gradient until the system becomes stable, i.e. until the operational point reaches the first stability region. In this way, strong gas puffing might trigger a transition from second to first $n = \infty$ ballooning stability with a subsequent reduction in the critical level of the pressure gradient. This topic will be discussed in more detail later in this paper.

For completeness, it should be mentioned that neutrals can affect ballooning stability in other ways than by changing magnetic shear via reducing the edge currents. For instance,

the presence of neutrals may modify the shear flow responsible for the formation of the ETB through charge exchange friction with ions [21].

4.2. Gas puff scan

In this section, the results of integrated transport modelling of a gas puff scan involving six different levels of neutral gas puffing are presented. The simulations have been performed using the coupled code COCONUT on a computational grid generated for JET shot 53298. The gas puff is injected at the midplane. Some results of the gas puff scan are presented in table 1. Figure 7 shows the ion density profiles in an outer midplane region covering the SOL, the ETB and part of the core for all six simulations in the scan. The separatrix is located at $R = 3.89$ m, where the density gradient changes. The other change in the density gradient visible in some of the profiles corresponds to the top of the ETB at $R = 3.855$ m. As explained

Table 1. Ion density at the separatrix, ion temperature at the separatrix and neutral particle flux through the separatrix as a function of the rate of neutral gas puffing in a number of COCONUT runs.

Puff rate Γ (s^{-1})	Separatrix ion density $n_i(\rho = 1)$ (m^{-3})	Separatrix ion temperature $T_i(\rho = 1)$ (eV)	Neutral flux through separatrix Γ_{in} (s^{-1})
0	0.87×10^{19}	593	32.58×10^{20}
2×10^{22}	2.95×10^{19}	354	9.07×10^{20}
4×10^{22}	4.40×10^{19}	297	6.09×10^{20}
6×10^{22}	6.65×10^{19}	239	8.74×10^{20}
8×10^{22}	7.67×10^{19}	193	5.62×10^{20}
10×10^{22}	8.39×10^{19}	178	4.18×10^{20}

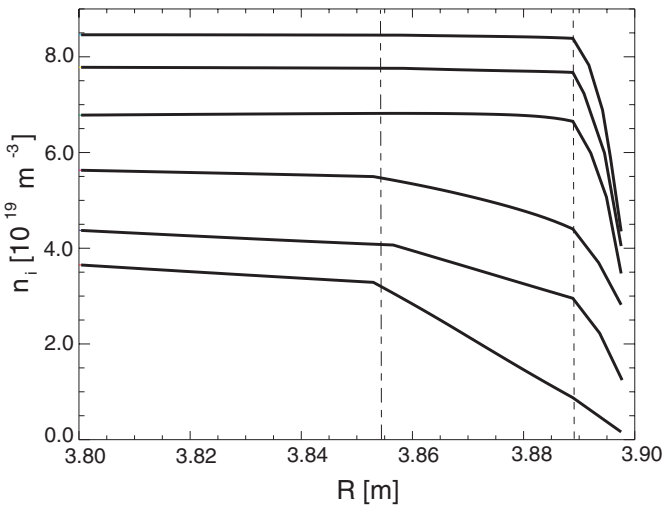

Figure 7. Ion density as a function of the major radius in integrated predictive simulations with different levels of external neutral gas puffing. Counting from top to bottom in the figure, the ion density profiles correspond are from simulations with the following levels of gas puffing: $\Gamma = 1 \times 10^{23}\,s^{-1}$, $\Gamma = 8 \times 10^{22}\,s^{-1}$, $\Gamma = 6 \times 10^{22}\,s^{-1}$, $\Gamma = 4 \times 10^{22}\,s^{-1}$, $\Gamma = 2 \times 10^{22}\,s^{-1}$ and $\Gamma = 0$. The position of the top of the ETB has been indicated with a chain line and the separatrix with a dashed line.

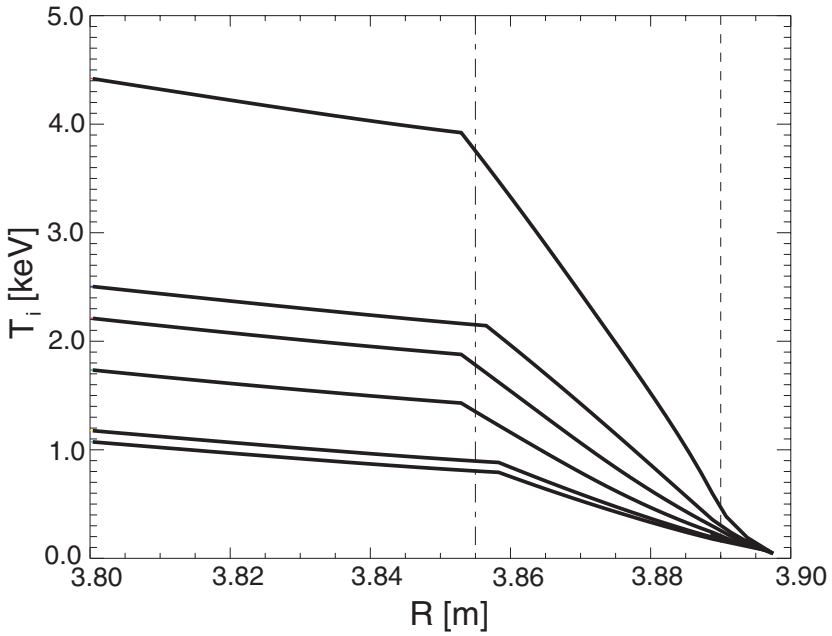

Figure 8. Ion temperature as a function of the major radius in integrated predictive simulations with different levels of external neutral gas puffing. Counting from top to bottom in the figure, the ion density profiles correspond are from simulations with the following levels of gas puffing: $\Gamma = 0$, $\Gamma = 2 \times 10^{22}\,\mathrm{s}^{-1}$, $\Gamma = 4 \times 10^{22}\,\mathrm{s}^{-1}$, $\Gamma = 6 \times 10^{22}\,\mathrm{s}^{-1}$, $\Gamma = 8 \times 10^{22}\,\mathrm{s}^{-1}$, $\Gamma = 1 \times 10^{23}\,\mathrm{s}^{-1}$ and $\Gamma = 0$. The position of the top of the ETB has been indicated with a chain line and the separatrix with a dashed line.

earlier, the edge density increases with increasing gas puffing, whereas the edge temperature and the neutral influx through the separatrix decrease. The corresponding ion temperature profiles are shown in figure 8.

Attention should be paid to the fact that the separatrix density reaches very high values for strong levels of gas puffing, e.g. $n_i(\rho = 1) = 8.4 \times 10^{19}\,\mathrm{m}^{-3}$ for a puff rate of $\Gamma = 1 \times 10^{23}\,\mathrm{s}^{-1}$. However, reliable experimental data on the edge density, against which the results could be compared, is scarce. At JET, there are basically two types of diagnostic data available for the edge density: Edge Lidar (Thomson scattering) data and target probe data, but both methods have a number of known problems. With edge Lidar, the position of the separatrix with respect to the data is not measured but reconstructed using the magnetic equilibrium code EFIT and the density gradient in the vicinity of the separatrix is large. Hence, the uncertainty of the measurements in the vicinity of the separatrix becomes large. The target probe data, on the other hand, exists only for the target regions. In order to obtain data for the outer midplane region, some kind of mapping technique has to be used.

The difficulty of comparing the predictive transport simulations with experimental data is illustrated in figure 9, which shows diagnostic data for the electron temperature and electron density, including core and edge Lidar, electron cyclotron emission spectroscopy (ECE) and lithium beam spectroscopy data, for discharge 53298 with no external gas fuelling. The electron temperature and electron density profiles calculated in the corresponding COCONUT simulation with no external gas puffing have also been plotted in figure 9 on top of the experimental data. It should be emphasized that the position of the experimental data points is uncertain by up to 2 cm. This is the level of uncertainty of the magnetic equilibrium code

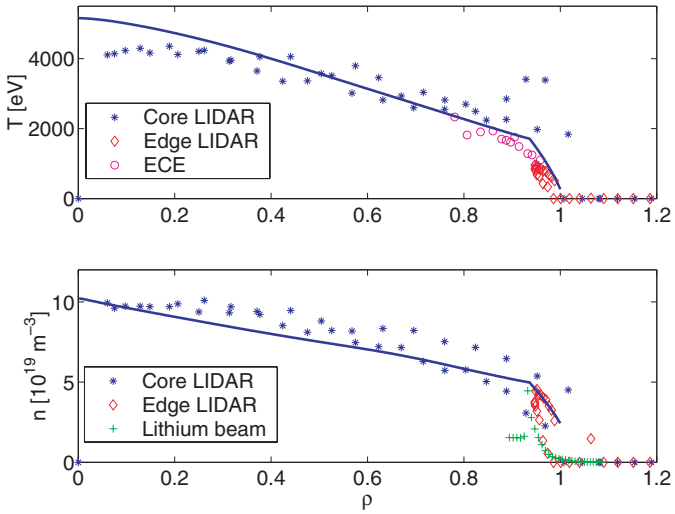

Figure 9. Diagnostic data for the electron temperature and electron density, including core and edge Lidar, ECE and lithium beam spectroscopy data, for discharge 53298. The electron temperature and electron density profiles calculated in the corresponding COCONUT simulation with no external gas fuelling have also been plotted on top of the experimental data. The uncertainty of the measured values is reported to be 10% for core Lidar, edge Lidar, ECE and lithium beam data. The uncertainty in the position of the data points attributable to the EFIT reconstruction is about 2 cm.

EFIT used to reconstruct the flux surfaces. Some misalignment between the experimental data points and the calculated profiles might even be inferred from the figure. Since the density and temperature gradients are steep at the edge, the uncertainty in the location of the separatrix with respect to the data points translates into large uncertainties in edge density and temperature. On top of the uncertainty in the position of the data points, it is reported that the uncertainty of the measured values is 10% for both edge Lidar, core Lidar, ECE and lithium beam spectroscopy. The separatrix densities obtained in the simulations easily fit into the range of uncertainty obtained from the experimental data. In the deep core, it is more straightforward to compare the simulation results with the available data. As shown in figure 9, the temperature and density profiles are predicted quite well in the core.

In order to investigate the possibility that the results of the integrated modelling would have been adversely affected by some inappropriately chosen simulation parameter, a sensitivity study with respect to a number of simulation parameters was carried out. To begin with, one of the COCONUT runs with modest gas puffing ($\Gamma = 4 \times 10^{22}\ \mathrm{s}^{-1}$) was matched by a stand-alone EDGE2D run using the heat fluxes from the COCONUT run as boundary conditions. Then, the following 'perturbations' were separately imposed on the starting scenario: the heat fluxes specified as boundary conditions were increased by up to three times, the transport coefficients given by COCONUT were also increased by up to three times, radiation from the SOL was increased by up to two times and recycling was reduced by up to 2.5%. For clarity, it should be stated that even a 2.5% reduction in recycling is quite significant. This can be understood by looking back at figure 4, which shows that the neutral flux penetrating the separatrix is up to two orders of magnitude smaller than the neutral influx into the SOL. Thus, a 2.5% change in the recycled neutral flux is of the same order of magnitude as the total neutral flux through the separatrix. In each of the extreme cases studied here, the effect on the density in the SOL was still modest. The largest reduction in the separatrix density resulted from increasing the transport coefficients three times and from reducing recycling by 2.5%, whereby the density

dropped by 20%. The change in heat fluxes and radiation caused the density to drop by less than 15%. These results show that the density obtained in the predictive transport simulations is not very sensitive to any other input parameter than the rate of gas puffing. It was also studied how the location and poloidal extent of the region with gas puffing affects the density in the SOL. Since the particles are relatively free to move along the field lines, the local density remains relatively insensitive to the poloidal location of the puffing region.

5. MHD stability analysis

Using MHD stability codes MISHKA and HELENA, MHD stability analysis was performed for some of the scenarios discussed in the preceding section. Three different levels of gas puffing were included in the MHD stability analysis: $\Gamma = 0$, $\Gamma = 4 \times 10^{22}\ \mathrm{s}^{-1}$ and $\Gamma = 1 \times 10^{23}\ \mathrm{s}^{-1}$. In order to maintain self-consistency, the analysis was based on the self-consistent COCONUT runs. To begin with, JETTO was run with the relevant separatrix values for the density and temperature given in table 1 as boundary conditions. In this way, the MHD stability analysis was done on fully self-consistent JETTO simulations. The dynamics of ELMs were not included in the analysis.

The results of the MHD stability analysis are illustrated in figures 10–12 corresponding to gas puffing rates $\Gamma = 0$, $\Gamma = 4 \times 10^{22}\ \mathrm{s}^{-1}$ and $\Gamma = 1 \times 10^{23}\ \mathrm{s}^{-1}$, respectively. The plots have been obtained by running HELENA and MISHKA on a set of equilibria obtained by repeatedly changing the edge pressure gradient and edge current within the ETB. Each combination of edge pressure gradient and edge current translates into a given level of magnetic shear. For each combination, the mode number of the most unstable peeling or finite n ballooning mode as calculated by MISHKA has been printed onto the plots in a co-ordinate system with the normalized pressure gradient α on the horizontal axis and magnetic shear s on the vertical one. Whenever no instabilities have been found, the relevant location on the plot has been left blank. In addition, the $n = \infty$ ballooning instabilities as calculated by HELENA have been marked with crosses on the plots. One can easily make out four distinct regions on the plots, each of which has been marked with a different shade of grey: a region with no instabilities,

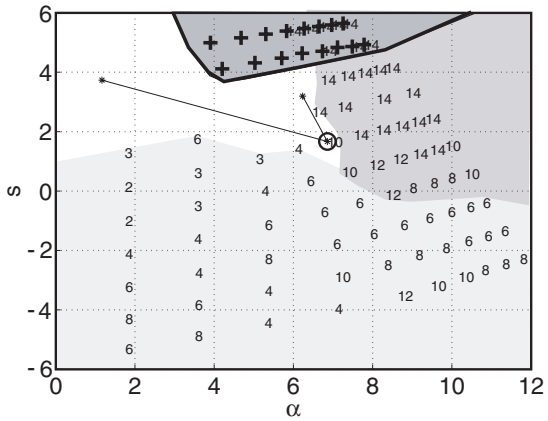

Figure 10. MHD stability diagram for the case with gas fuelling $\Gamma = 0$. The numbers indicate the mode number of the most unstable mode. The $n = \infty$ ballooning unstable region has been marked with crosses. The operational point has been plotted for $\rho = 0.92, 0.95$ and 0.99. The location of the top of the ETB at $\rho = 0.95$ has been marked with a circle.

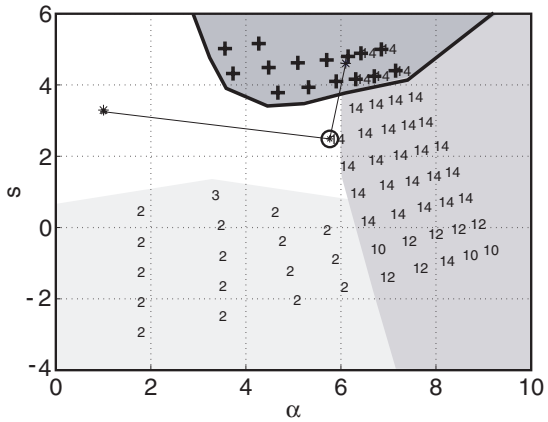

Figure 11. MHD stability diagram for the case with gas fuelling $\Gamma = 4 \times 10^{22}\ \mathrm{s}^{-1}$. The notation in the figure is to be interpreted as in figure 10. The operational point has been plotted for $\rho = 0.92$, 0.95 and 0.98.

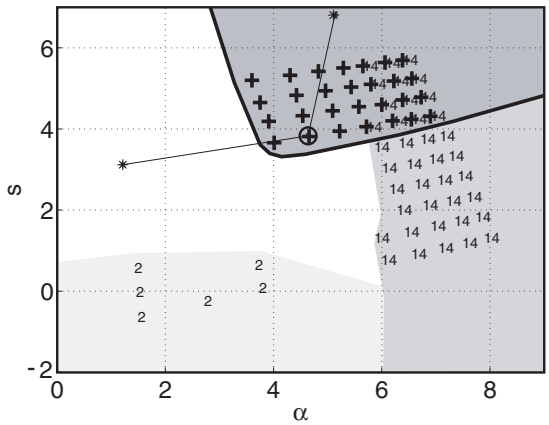

Figure 12. MHD stability diagram for the case with gas fuelling $\Gamma = 1 \times 10^{23}\ \mathrm{s}^{-1}$. The notation in the figure is to be interpreted as in figure 10. The operational point has been plotted for $\rho = 0.92$, 0.95 and 0.98.

a region in which the low n kink instability is dominant, a region in which the medium n ballooning/peeling instability dominates and the $n = \infty$ ballooning unstable region. In most cases, the latter two regions partially overlap each other. Finally, the plots show the location of the operational point, i.e. the point with unperturbed edge current and edge density, for a few different magnetic surfaces.

A few things should be noted. First, the MHD stability analysis done with MISHKA has been limited to toroidal mode numbers n smaller than or equal to 14 in order to keep the amount of computing time within reasonable limits. The computing time and memory requirements namely increase with the square of n, so that it quickly becomes more and more demanding to do the analysis for higher and higher mode numbers. Because of the limited range of the analysis, it is quite probable that $n = 14$ is not actually the most unstable mode in all the cases indicated on the plots. It can be expected that some mode with higher mode number is actually more unstable at many of the locations marked with an $n = 14$ instability. Second, it

should be noted that the stability diagram varies slightly as a function of the magnetic surface, so that the stability boundaries look slightly different for each magnetic surface. Shown is the stability diagram for $\rho = 0.95$, which corresponds to the top of the ETB.

When comparing figures 10–12, one should keep in mind the conclusions of section 4.1, such as the fact that increasing gas puffing leads to decreasing bootstrap current and total edge current and increasing magnetic shear. Indeed, the case with zero gas puffing illustrated by figure 10 is very kink unstable, because the edge current is high due to the low edge density. However, despite the strong kink instability there is still a gap with access to second $n = \infty$ ballooning stability, but it closes for $s < 2$. For increasing ρ, the operational point moves from the first ballooning stability region into the second ballooning stability region without touching the $n = \infty$ ballooning stability limit. The system remains in the second stability region for all magnetic surfaces within the ETB. The maximum operational α obtained in this scenario is limited by a region of finite n ballooning/peeling instability.

In figure 11 corresponding to the scenario with the intermediate level of gas puffing, the system is more kink stable, because the edge current is significantly smaller than in the case with zero gas fuelling. Access to second stability opens readily, since the kink modes are more stable. Again, the maximum operational α, in this case $\alpha \approx 6$, is defined by a region of $n = 14$ ballooning instability. The radial localization of these modes is approximately equal to the width of the ETB. For the magnetic surface corresponding to the top of the ETB, the system is in the second stability region. However, because the edge current is small, magnetic shear increases dramatically at the edge. Therefore, the plasma is $n = \infty$ ballooning unstable at the very edge. Indeed, it seems to be a ubiquitous feature that the edge ($\rho > 0.97$) is always unstable for an intermediate or strong level of gas puffing. This causes ELM activity resembling the experimentally observed mixed type I–II ELMy H-mode in JET [23], as will be discussed later.

In the case with the strongest gas fuelling illustrated by figure 12, the edge current is vanishingly small everywhere within the ETB, whereby magnetic shear is strong. Therefore, the operational point is pushed directly from the first stability region into the ideal ballooning unstable region. The whole ETB is unstable. It should also be noted that the kink modes are further stabilized because of the small edge current, so that, in principle, access to second stability is opened, but for a much reduced level of magnetic shear.

It should be noted that, in the past, Saibene *et al* [24] discussed a gas puffing scan with low- and medium-triangularity JET discharges, including a transition from type I to type III ELMs, reporting that a type I ELMy H-mode discharge with a low level of gas puffing did not enter second stability. A similar conclusion was drawn in [16], although a transition to the second stability region was not ruled out in this paper. However, it should be remembered that neither satisfactory diagnostics nor good enough self-consistent equilibria were available when this result was obtained. Since then, diagnostics have improved significantly and self-consistent ESCO equilibria can be used in JETTO instead of the previously used EFIT equilibria. The improvement in diagnostics and equilibria has led to the more recent understanding presented here that type I ELMy H-mode discharges do enter second stability. Another difference that should be mentioned is that the lack of access to second stability was obtained for rather low triangularity, $\delta = 0.21$. Using MISHKA, it has recently been shown that high-triangularity eases access to second stability [15]. This is because low n kink modes gradually close the access to second stability when triangularity decreases.

Interpretative modelling, too, supports the current understanding that type I ELMy H-mode discharges enter second stability, whereas type III ELMy H-mode discharges stay in first stability. In order to illustrate this point, interpretative modelling of two diagnostically optimized configuration (DOC) JET discharges, i.e. discharges with the best available

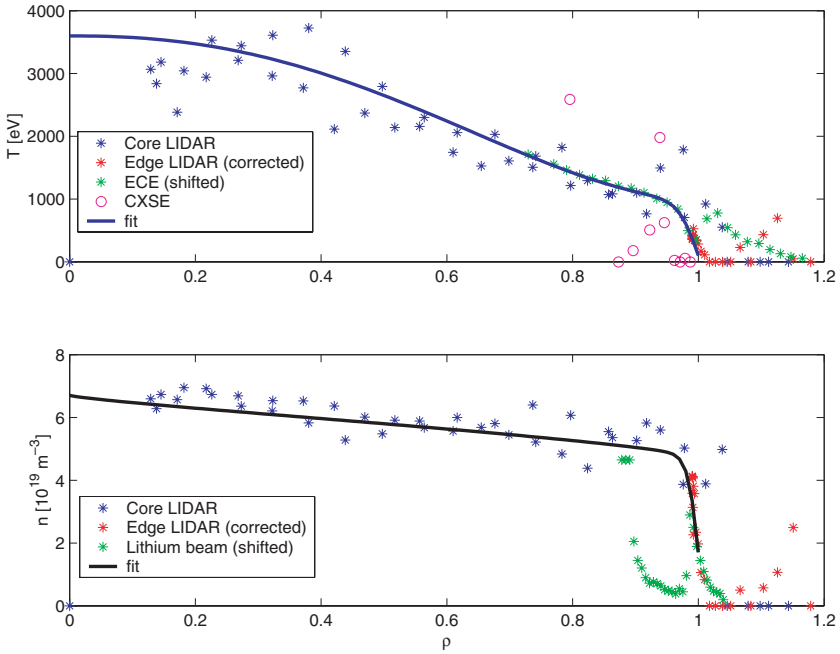

Figure 13. Profiles fitted to the experimental temperature and density data for the DOC type I ELMy H-mode JET discharge 55973 used in an interpretative JETTO simulation. Diagnostics used for the temperature are core and edge Lidar, ECE and CXSE (charge exchange recombination spectroscopy). Diagnostics used for the density are core and edge Lidar and lithium beam spectroscopy.

diagnostics, will be considered. One of them, discharge 55973, is a type I ELMy H-mode discharge, whereas the other one, discharge 55974, is a type III ELMy H-mode discharge. Both shots have a triangularity of about $\delta = 0.4$. In the interpretative simulations, the density and temperature profiles are taken from experimental data, whereas the current is predicted. Figures 13 and 14 show the temperature and density profiles that have been fitted to the experimental data and used in the interpretative JETTO runs for shots 55973 and 55974, respectively. The experimental data consists of edge and core Lidar data for both temperature and density, charge exchange recombination spectrometry data for the temperature and lithium beam data for the density. Figures 15 and 16 illustrate the results of MHD stability analysis with MISHKA and HELENA for the interpretative JETTO runs on shots 55973 and 55974, respectively. Shown here in the α–s co-ordinate system is the usual ballooning stability picture with mode numbers of the most unstable finite n kink/peeling and ballooning modes and the ideal ballooning unstable region together with the operational point. The figures are for the magnetic surface $\rho = 0.97$, which is well within the ETB. Clearly, discharge 55973 with type I ELMs enters second stability, whereas discharge 55974 with type III ELMs stays in first stability. This modelling of experimental shots with the best available diagnostic data shows quite convincingly that a type I ELMy H-mode discharge can enter second stability, as proposed in the discussion on predictive modelling.

5.1. Transition from second to first ballooning stability

As discussed earlier, the plasma cannot remain in a state with a combination of pressure gradient and magnetic shear that results in an MHD instability. For the case with the strongest gas

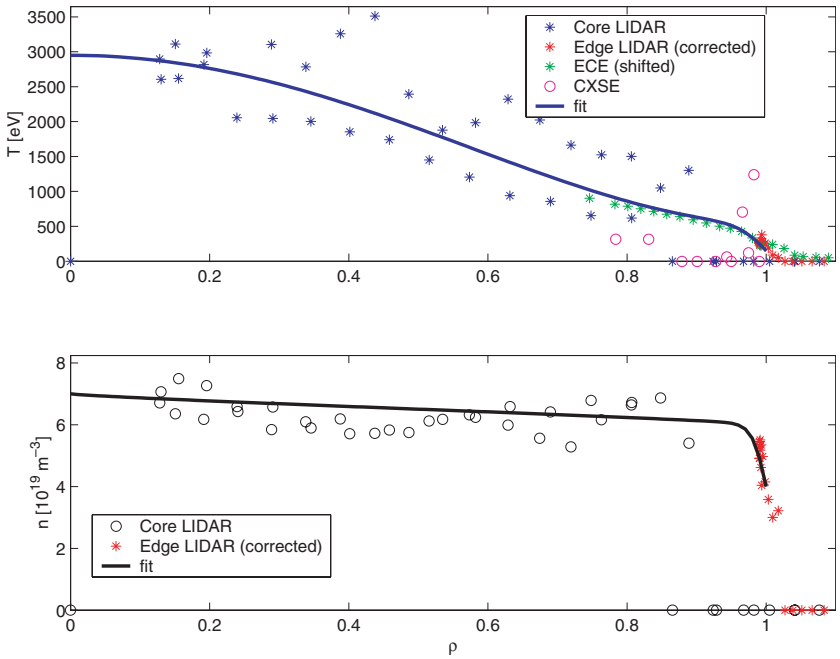

Figure 14. Profiles fitted to the experimental temperature and density data for the DOC type III ELMy H-mode JET discharge 55974 used in an interpretative JETTO simulation. Diagnostics used for the temperature are core and edge Lidar, ECE and CXSE. Diagnostics used for the density are core and edge Lidar and lithium beam spectroscopy.

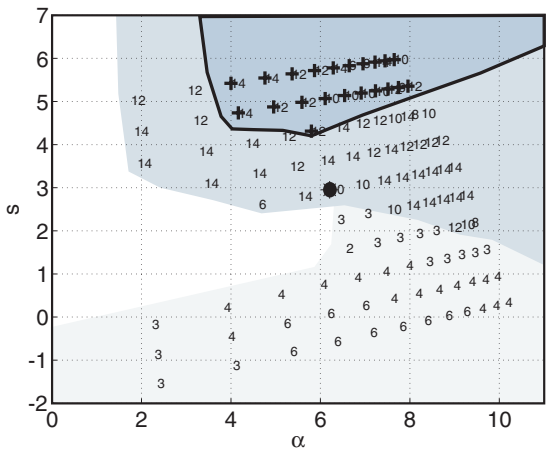

Figure 15. MHD stability diagram for the magnetic surface $\rho = 0.97$ for an interpretative JETTO simulation of JET discharge 55973. The notation in the figure is to be interpreted as in figure 10. The operational point is indicated with a large dot.

fuelling illustrated by figure 12, this would mean that the pressure gradient would actually never exceed the first stability limit at $\alpha \approx 3.5$ due to the triggering of ELMs. Thus, the operational point would always be in the first ballooning stability region. Similarly, the operational point would remain in the second ballooning stability region for magnetic surfaces within the ETB

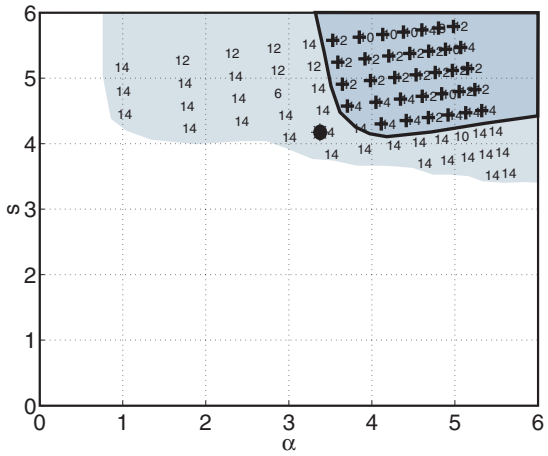

Figure 16. MHD stability diagram for the magnetic surface $\rho = 0.97$ for an interpretative JETTO simulation of JET discharge 55973. The notation in the figure is to be interpreted as in figure 10. The operational point is indicated with a large dot.

in the scenarios with lower levels of gas fuelling illustrated by figures 10 and 11. As magnetic shear is lower in these cases, the pressure gradient can take values up to $\alpha \approx 6$ defined by the finite n ballooning stability limit. From the discussion here, it is clear that an increase from low to high levels of neutral gas puffing at some point causes the operational point to move from the second to the first ballooning stability region, whichever part of the ETB is considered. Qualitatively, this means that a sufficiently strong increase in neutral gas puffing can trigger a transition from second to first ballooning stability.

The dynamics of the transition from second to first ballooning stability has been investigated with JETTO by varying the level of gas puffing and using a critical pressure gradient corresponding to the relevant stability limit. A run with modest gas puffing $\Gamma = 2 \times 10^{22}\,\mathrm{s}^{-1}$ and critical pressure gradient $\alpha_c = 6$ corresponding to the finite n ballooning stability limit has been compared with a run with strong gas puffing $\Gamma = 1 \times 10^{23}\,\mathrm{s}^{-1}$ and critical pressure gradient $\alpha_c = 3.5$ corresponding to the first stability limit. The ELM frequency in the latter case is about an order of magnitude larger than in the former case. This is illustrated in figure 17, which shows the ion thermal conductivity χ_i as a function of time for both cases in frames (a) and (b), respectively. It is easy to understand why the ELMs necessarily become more frequent for a smaller value of the critical pressure gradient: the smaller the critical pressure gradient is, the less time it takes for the pressure gradient to build up to the critical value. The increase in ELM frequency is accompanied by a deterioration of plasma confinement. Frames (c) and (d) in figure 17 show the plasma thermal energy content and the confinement factor H89, respectively, for the two cases. The confinement factor H89 is defined as $\tau_r/\tau_{\mathrm{ITER}}$, where τ_r is the energy replacement time and τ_{ITER} is the ITER-89P confinement time. Both the energy content and confinement factor drop by approximately 30% when going from low to high gas puffing.

The increase in ELM frequency and deterioration of plasma confinement seen in the simulations is very similar to what has been observed in experiments with strong gas puffing. Hence, it can be inferred that it might be possible to qualitatively explain the experimentally observed transition from type I to type III ELMy H-mode triggered by strong gas puffing as a transition from second to first ballooning stability. The experimentally observed increase in ELM frequency could then be due to the fact that the inherent critical pressure gradient

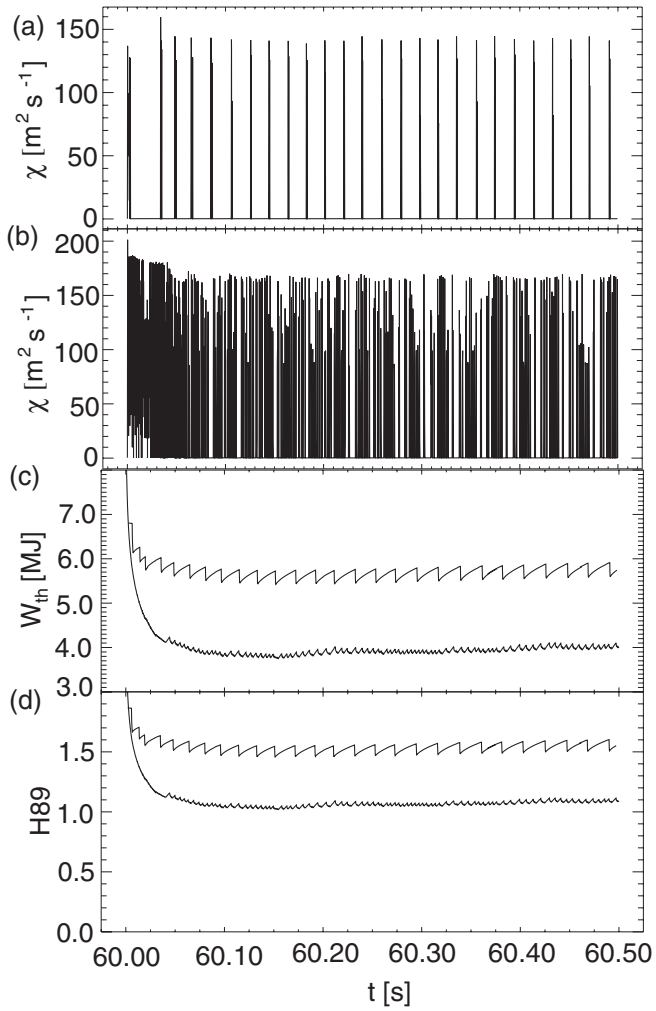

Figure 17. Ion thermal conductivity, plasma thermal energy content and confinement factor H89 as a function of time in two JETTO simulations. (*a*) Ion thermal conductivity for gas puffing $\Gamma = 2 \times 10^{22}\,\mathrm{s}^{-1}$ and critical pressure gradient $\alpha_c = 6$. (*b*) Ion thermal conductivity for gas puffing $\Gamma = 1 \times 10^{23}\,\mathrm{s}^{-1}$ and critical pressure gradient $\alpha_c = 3.5$. The ELM frequencies in frames (*a*) and (*b*) are about 50 Hz and 500 Hz, respectively. (*c*) Energy content for case (a) (upper curve) and case (*b*) (lower curve). (*d*) Confinement factor H89 for case (a) (upper curve) and case (b) (lower curve).

of the system decreases in the transition from second to first ballooning stability. Finally, it might as well be possible to explain the deterioration in plasma confinement associated with the transition from type I to type III ELMs by a decrease in the edge pressure gradient, which translates into a lower core temperature due to profile stiffness and hence reduces the thermal energy content. This model can thus, even in its ideal formulation, explain some of the most important characteristics of a type III ELMy H-mode, such as the increase in ELM frequency and deterioration of plasma confinement with respect to a type I ELMy H-mode, and thereby provide an explanation for many experimental situations with type III ELMs.

It is worth noting that in many experiments type III ELMs are characterized by an ELM frequency that decreases with power [25], which is a feature that the *ad hoc* model used here

in itself does not easily reproduce in ideal MHD. Nevertheless, the model used in the previous analysis can easily be extended so that the first ballooning stability boundary is controlled by resistive rather than ideal ballooning modes, which can be the case in highly collisional plasma [26]. This could further reduce the achievable level of critical pressure gradient below $\alpha \approx 3.5$ at the first ballooning stability limit. The effects of resistivity could help to explain the experimental observation that the ELM frequency decreases with increasing power in type III ELMy H-mode.

5.2. Mixed type I-II ELMy H-mode

As mentioned before, the result illustrated in figure 11 implies a possible explanation for experimentally observed mixed type I-II ELMy H-mode activity. Stability at the very edge is limited by the first ballooning stability limit, whereas the finite n stability limit applies deeper inside the ETB, situations that result in type II and type I ELMs, respectively. In this model, the distinction between type II and type III ELMs is related to the radial depth of the ideal ballooning unstable region: the ELMs due to the $n = \infty$ ballooning instability are here defined to be type III ELMs, if stability in the whole ETB is determined by the first stability limit, and type II ELMs, if the first stability limit applies only to the outermost edge. As will be shown later, this definition is justified, because the type II ELMs seen here do not cause a significant deterioration of plasma confinement, whereas the type III ELMs do.

In order to simulate plasmas with mixed type I-II ELMy H-mode, the following modification was made to the ELM model in JETTO: the ETB was radially divided into two regions, an inner region corresponding to the part of the ETB in the second stability region in figure 11 and an outer region corresponding to the unstable edge. Here, the boundary between the regions was set at $\rho = 0.99$. In accordance with the previous discussion on the behaviour of the critical pressure gradient, $\alpha_c = 6.0$ was used in the inner region and $\alpha_c = 3.5$ in the outer region. The enhancement of transport due to ELMs originating in the inner region was applied over the whole ETB, whereas the ELMs in the outer region were mostly confined to the outer region. This is consistent with the understanding that the $n = \infty$ ballooning modes limiting stability near the very edge are more localized for strong shear than the finite n ballooning modes determining stability closer to the top of the ETB, which can be justified as follows.

Reference [27] gives an expression for the width of the envelope of coupled harmonics forming a balloning mode eigenfunction in the high n limit with the maximum pressure gradient at the plasma edge:

$$A(x) = \exp\left(-\frac{1}{2}|v'(\theta_0)|\left(\frac{\partial^2\omega^2/\partial\psi^2}{\partial^2\omega^2/\partial\theta_0^2}\right)^{1/2}x^2\right). \tag{2}$$

Here, $|v'(\theta_0)| = \mathrm{d}q/\mathrm{d}\psi = q'$ is the derivative of the safety factor with respect to the poloidal flux co-ordinate ψ, ω^2 is the local oscillation frequency of an individual harmonic, θ_0 is the toroidal location of the instability and $x = n^{1/2}(\psi - \psi_0)$, where ψ_0 is the location of the minimum of ω^2. Assuming that $\partial^2\omega^2/\partial\theta_0^2 \sim \omega^2$ and $\partial^2\omega^2/\partial\psi^2 \sim \omega^2/(\Delta\psi_{\mathrm{ETB}})^2$, where $\Delta\psi_{\mathrm{ETB}}$ is the pedestal width, the envelope width can be written as

$$A(\psi) = \exp\left(-\frac{1}{2}\frac{nq'}{\Delta\psi_{\mathrm{ETB}}}(\psi - \psi_0)^2\right). \tag{3}$$

The width of the envelope thus scales as

$$\Delta\psi_{\mathrm{envelope}} \sim \sqrt{\frac{\Delta\psi_{\mathrm{ETB}}}{nq'}}. \tag{4}$$

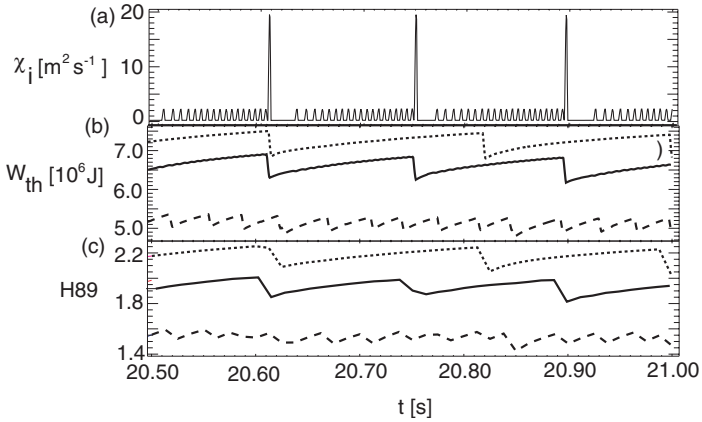

Figure 18. Mixed type I-II ELMy H-mode obtained in a JETTO simulation with a moderate level of gas puffing ($\Gamma = 4 \times 10^{22}$ s^{-1}). The ETB was split into two parts: an inner region with $\alpha_c = 6.0$ and an outer region with $\alpha_c = 3.5$. (*a*) Ion thermal conductivity near the edge at $\rho = 0.995$ as a function of time, clearly showing both frequent small-amplitude type II ELMs and large-amplitude type I ELMs. (*b*) Plasma energy content as a function of time. For comparison, the dotted curve corresponds to a simulation with pure type I ELMy H-mode ($\alpha_c = 6.0$) and the dashed curve to a simulation with pure type III ELMy H-mode ($\alpha_c = 3.5$). (*c*) Confinement factor H89 as a function of time. Again, the results for a case with type I ELMy H-mode (· · · · · ·) and type III ELMy H-mode (- - - -) have been included.

This shows that ballooning modes become very localized in the high n limit and for strong magnetic shear at the edge. Recent work suggests that low and medium n ballooning modes, on the other hand, usually occupy the whole pedestal [11].

Using the ELM model described here, it was possible to qualitatively reproduce the experimentally observed mixed type I-II ELMy H-mode in stand-alone JETTO simulations. The result is shown in figure 18, which is from a simulation with the intermediate level of gas puffing $\Gamma = 4 \times 10^{22}$ s^{-1}. Frame (*a*) shows the ion thermal conductivity near the edge at $\rho = 0.995$ as a function of time. The frequent small-amplitude type II ELMs occur in the edge region of the ETB with $\alpha_c = 3.5$, whereas the less frequent large-amplitude type I ELMs originate in the inner region of the ETB with $\alpha_c = 6.0$.

Frame (*b*) in figure 18 shows the energy content of the plasma as a function of time. The 'large' type I ELMs remove about 8.5% of the plasma energy per ELM. The energy loss due to the 'small' type II ELMs, barely visible in the figure, is much smaller, typically about 0.1% per ELM. However, the type II ELMs still play a role in controlling the energy content, because their frequency is significantly larger than the type I ELM frequency. The behaviour described here is characteristic for a model with the type I ELMs covering the whole ETB and the type II ELMs only the very edge, as well as qualitatively similar to experimental behaviour. The plasma energy content in the simulation with mixed type I-II ELMy H-mode has been compared to that in simulations corresponding to pure type I ELMy H-mode ($\alpha_c = 6.0$) and pure type III ELMy H-mode ($\alpha_c = 3.5$), as illustrated in frame (*b*) in figure 18. The comparison demonstrates that the energy content of the plasma in the case with mixed type I-II ELMs is some 10% lower than in the case with pure type I ELMs, but some 40% higher than in the case with pure type III ELMs. Frame (*c*) shows the confinement factor H89 as a function of time and a similar comparison as in frame (*c*) for the three different types of ELMy H-mode plasma. Again, the same trends are evident, i.e. a modest deterioration of confinement for mixed type I-II ELMy H-mode with respect to pure type I ELMy H-mode plasma, but significantly better confinement than in type III H-mode plasma. These observations are consistent with

experiments, suggesting that the situation with the whole ETB controlled by the first stability limit indeed corresponds to type III ELMs and the situation with only the very edge controlled by this stability limit to type II ELMs. A more detailed discussion of mixed type I-II ELMy H-mode will follow elsewhere.

Experimentally, mixed type I-II ELMy H-mode has been observed in very narrow ranges of density and power. A slight increase in power, or equivalently a slight decrease in density, causes a mixed type I-II ELMy H-mode to transfer into a pure type I ELMy H-mode, whereas, a slight decrease in power, or similarly a slight increase in density, causes it to transfer into a pure type III ELMy H-mode. JETTO modelling combined with MHD stability analysis reproduces this result by showing what happens to edge stability for small changes in power and density: a small increase in power or decrease in density pushes the unstable operational point at the very edge back into the second ballooning stability region, i.e. the situation transforms into a pure type I ELMy H-mode in the present model. A small decrease in power or increase in density, on the other hand, causes the whole pedestal to become infinite n ballooning unstable, i.e. the situation transforms into a pure type III ELMy H-mode.

6. Summary and discussion

In this paper, integrated predictive modelling of ELMy H-mode JET plasmas has been performed using the integrated transport code COCONUT, which is a coupling of the JET transport codes EDGE2D and JETTO for edge (SOL) and core modelling, respectively. Integrated modelling is needed, because separate stand-alone core and edge modelling does not yield self-consistent results. It has been shown through integrated predictive modelling that external gas fuelling can very sensitively affect ballooning and peeling/kink stability via its influence on edge density, collisionality, bootstrap current, total edge current and magnetic shear. Modelling with COCONUT also shows that very high edge densities can be reached with strong external gas fuelling. Moreover, the modelling also reveals that only a minor fraction of the total neutral gas puff injected at the edge actually penetrates all the way through the separatrix. The simulation results are consistent with the experimental data that is available for scenarios resembling those simulated here. However, the accuracy of the edge data for JET is poor, largely due to the uncertainty in the position of the separatrix.

MHD stability analysis has been performed on JETTO runs using boundary conditions calculated self-consistently by COCONUT. It has been shown that the plasma can gain access to second $n = \infty$ ballooning stability in many cases, such as with modest gas puffing. The transition to second stability can be controlled either by the peeling and the finite n ballooning modes or by infinite n ballooning stability. It has also been demonstrated that strong gas puffing can trigger a transition from second to first ballooning stability, which causes a dramatic decrease in the inherent critical pressure gradient of the system. As a result of this, the ELM frequency increases dramatically. The result implies that it might be possible to explain the experimentally observed transition from type I to type III ELMy H-mode triggered by strong gas puffing as well as the subsequent increase in ELM frequency and deterioration of plasma confinement as a transition from second to first stability (either ideal or resistive). Furthermore, it has been possible to qualitatively reproduce the experimentally observed mixed type I-II ELMy H-mode in transport simulations.

Acknowledgment

This work has been performed under the European Fusion Development Agreement.

References

[1] Huysmans G T A, Hender T and Alper B 1998 *Nucl. Fusion* **38** 179
[2] Connor J W, Hastie R J, Wilson H R and Miller R L 1998 *Phys. Plasmas* **5** 2687
[3] Rogers B N and Drake J F 1999 *Phys. Plasmas* **6** 2797
[4] Hastie R J, Catto P J and Ramos J J 2000 *Phys. Plasmas* **7** 4561
[5] Snyder P B *et al* 2002 *Phys. Plasmas* **9** 2037
[6] Dimits A M *et al* 2000 *Phys. Plasmas* **7** 969
[7] Saibene G *et al* 2001 *Proc. 28th EPS Conf. on Plasma Physics and Controlled Fusion (Madeira, Portugal, 18–22 June 2001)*
[8] Cennachi G and Taroni A 1988 JET-IR(88)03
[9] Simonini R *et al* 1994 *Contrib. Plasma Phys.* **34** 368
[10] Mikhailovskii A B *et al* 1997 *Plasma Phys. Rep.* **23** 844
[11] Huysmans G T A, Sharapov S E, Mikhailovskii A B and Kerner W 2001 *Phys. Plasmas* **10** 4292
[12] Erba M *et al* 1997 *Plasma Phys. Control. Fusion* **39** 261
[13] Houlberg W A, Shaing K C, Hirshman S P and Zarnstorff M C 1997 *Phys. Plasmas* **4** 3231
[14] Onjun T, Kritz A, Bateman G and Parail V 2003 *Proc. 11th Int. Congress on Plasma Physics (Sydney 15–19 July 2002)*
[15] Onjun T, Bateman G, Kritz A H and Hammet G 2002 *Phys. Plasmas* **9** 5018
[16] Parail V V *et al* 2000 *Proc. 27th EPS Conf. on Plasma Physics and Controlled Fusion (Budapest, Hungary, 19–23 June 2000)*
[17] Heikkinen J A *et al* 2001 *J. Comp. Phys.* **173** 527
[18] Fundamenski W *et al* 2003 *Proc. 15th PSI Conf. (Gifu, Japan, May 2002) J. Nucl. Matter* at press
[19] JET Team (presented by A. Taroni) 1996 *Proc. 16th IAEA International Conf. on Fusion Energy (Montreal, Canada, 7–11 October 1996)* vol 2, p 477
[20] ITER Physics Experts Groups on Confinement and Confinement and Transport Modelling and Database, ITER Physics Basis Editors, ITER EDA 1999 *Nucl. Fusion* **39** 2175
[21] Carreras B A *et al* 1998 *Phys. Plasmas* **5** 2623
[22] Fukada T *et al* 2000 *Plasma Phys. Control. Fusion* **42** A289
[23] Saibene G, Sartori R, Loarte A *et al* 2002 *Plasma Phys. Control. Fusion* **44** 176a
[24] Saibene G *et al* 1999 *Nucl. Fusion* **39** 1133
[25] Chankin A V and Saibene G 1999 *Plasma Phys. Control. Fusion* **41** 913
[26] Glasser A H, Greene J M and Johnson J L 1975 *Phys. Fluids* **18** 875
[27] Connor J W, Hastie R J and Taylor J B 1979 *Proc. R. Soc.* A **365** 1